ADVANCED FUNCTIONAL MATERIALS
www.afm-journal.de

Growth of Vertically Aligned Tunable Polyaniline on Graphene/ZrO_2 Nanocomposites for Supercapacitor Energy-Storage Application

*Soumen Giri, Debasis Ghosh, and Chapal Kumar Das**

In-situ hydrothermal method is employed to synthesize graphene/zirconium oxide composite from respective precursors graphene oxide and zirconium oxy-nitrate. In this method, the graphene oxide is reduced itself to graphene and simultaneously metal oxide gets anchor on the graphene sheets. A novel method is also developed for the preparation of vertically aligned tunable polyaniline on the graphene/zirconium oxide nanocomposite, which leads to achieve high surface area (207.1 $m^2 g^{-1}$), high electrical conductivity (70.8 S cm^{-1}), high specific capacitance (1359.99 Fg^{-1} at 1 mV s^{-1}), and high electrochemical performances as supercapacitor electrode materials. This vertically aligned conducting polymer gets easy contact with electrolyte ions and provides numerous redox active sites during charging and discharging. Moreover, such a simple and low cost assembly approach can be a pioneer for the large-scale production of various functional architectures for energy storage and conversions.

1. Introduction

With the rising progress of global economy and industry, the impending energy crisis has stimulated intense research on the low cost, environmentally friendly, and renewable energy resources.[1] Therefore, great efforts have been devoted to develop low cost electrode materials with high energy density, high power density, and excellent cycling stability. Supercapacitors, can be considered as the supreme candidate of the next-generation energy storage/conversion systems with the unique ability to store energy in a fraction of second and delivering the stored energy rapid enough than any other conventional energy storage devices. It also ensures high power density when coupled with batteries or fuel cells.[1–4] However, the supercapacitors suffer from low working potential that result in low energy density than conventional batteries. So, it's essential to improve their performances to encounter the higher requirements of future technologies by developing new materials with the interfaces at the nanoscale dimension. Lower specific energy of electrochemical double layer capacitors (EDLCs) with respect to the batteries and lower power densities of pseudocapacitors than EDLCs has motivated to develop the better performance characteristics hybrid supercapacitors. These hybrid supercapacitors use both Faradaic and non-Faradaic processes to store charge and thereby have achieved higher energy density and moderated power density accompanied with high cycling stability and thus have restricted the monopolism of pseudocapacitor.

Intense research has established that combination of the micro structured carbonaceous materials with electroactive materials into a single system can take the benefits of both the double layer capacitance and pseudocapacitance arising from the synergistic interaction of the two. In this sense, graphene is the most interesting carbonaceous material with ultra-high surface area (2600 $m^2 g^{-1}$), excellent electric conductivity, two-dimensional sp^2 carbon arrangement with one-atom thickness. However, the strong electrostatic interaction amongst the graphene sheets leads to restacking of the sheets resulting in lower specific surface area and lower capacitance.[5] This drawbacks can be overcome by functionalization on the surface or incorporating nanocrystals in form of nanocomposites. The conducting polymers and transition metal oxides are two typical pseudocapacitive materials, which are capable of storing more charges than carbonaceous materials, but are limited by their poor stability and high resistance during cycling. The conducting polymer is frequently used into supercapacitor materials for obtaining the efficient charge storage and delivery which strongly depends on the orientation of polymer chains into inorganic host. The polymer molecules are directed to grow along the large oriented tunnels of 3D hosts or interlayer space of the 2D hosts where the structurally organized frameworks are provided by the inorganic host.[6] But, main problem is that nanoparticles tend to self-aggregate due to their high surface energy which effectively reduces the contact area amongst the active materials, conductive materials, and electrolyte. So, it is very much essential to preserve the maximum available surface area of the active nanomaterials for their full utilizations. Recently, different types of hierarchical building blocks have been synthesized at the nanoscale as a new class of electrode materials, which synergistically enhance the features of both micromaterials and nanomaterials. In such structures,

S. Giri, D. Ghosh, Prof. C. K. Das
Materials Science Centre
Indian Institute of Technology Kharagpur
Kharagpur, 721302, India
E-mail: chapal12@yahoo.co.in

DOI: 10.1002/adfm.201302158

the nanoscale dimension of building blocks stimulates the kinetics of charge storage by shortening the diffusion paths, while the primary architecture at the nanoscale effectively avoids aggregation of the active nanomaterials and facilitates the transport of electrons and ions.[7,8]

Amongst the various methods for preparation of graphene based composites of nanomaterials, mostly the mechanical mixing is followed; however this method suffers from the inhomogeneous dispersion of the nanoparticles over graphene sheets and sometimes graphene sheets are separated out. The widely used method for the synthesis of graphene involves the reduction of graphene oxide (GO) using hydrazine (N_2H_4) as reductant. But unfortunately, this chemical approach results in high sheet resistance, which restricts their practical applications. Furthermore, N_2H_4 is a toxic reagent which fails to reduce GO completely and also introduce some impurity as C–N bonding in graphene framework.[9]

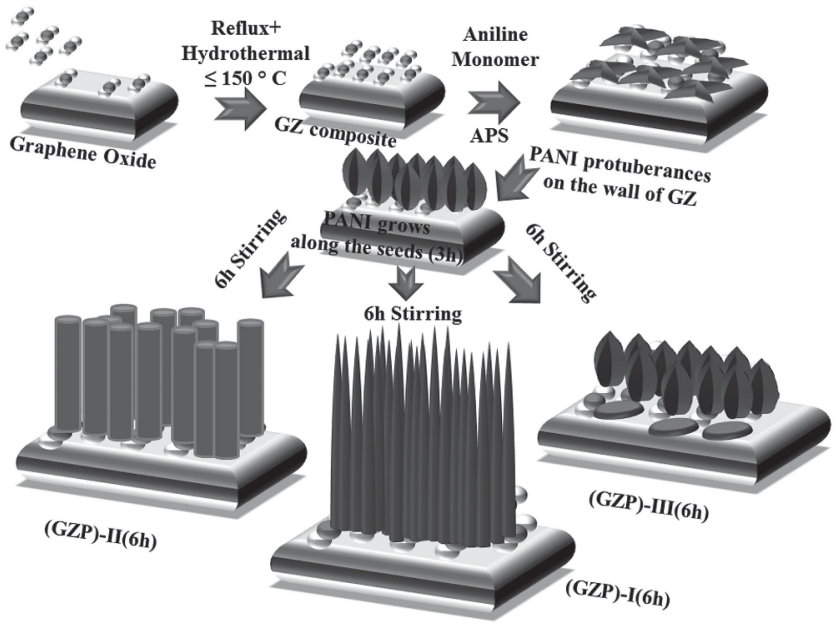

Scheme 1. Scheme for the hydrothermal synthesis of GZ composite and fabrication of vertically aligned PANI nanofibres through facile polymerization of aniline monomer on GZ composite.

Avoiding any type of limitation, we have used a simple process for the in-situ reduction of GO using $ZrO(NO_3)_2$ as reducing agent. During reduction $ZrO(NO_3)_2$ converts to ZrO_2 and attached with reduced graphene oxide forming graphene/ZrO_2 (GZ) nanocomposite. Additionally, Zirconium oxide (ZrO_2) is an attractive material in many fields because of its excellent mechanical, thermal, and optical properties.[10] Herein, we have synthesized ternary composite by combining the graphene/ZrO_2 and polyaniline (GZP) in a tunable way where orientation of polyaniline is also effective for charge storage and delivery. Our proposed route for the synthesis of vertically aligned PANI on graphene/ZrO_2 surface, where ZrO_2 are embedded in between graphene and the PANI matrix is believed to be a significant innovation for developing novel electrode materials with improved electrochemical performances.

2. Results and Discussion

2.1. Preparation and Characterization of GZ and GZP Composites

In this article, we have proposed a novel strategy to synthesize vertically align polyaniline on GZ in a mild condition (≤150 °C), as shown in **Scheme 1**. Starting from the $ZrO(NO_3)_2$ precursor, GZ was obtained by successive way of sonication, reflux, and hydrothermal treatment with GO. The oxidation polymerization of aniline on ZrO_2 surface occurs in acidic conditions. A series of GZP nanocomposites were prepared using different weight ratio of GZ (binary composite) to aniline monomer and changing the polymerization time. The as prepared nanocomposites using weight ratio of GZ to aniline monomer (1:1) for 3 h polymerization, (1:1), (0.5:1), and (1:0.5) for 6 h polymerization have been leveled as GZP-I(3 h),GZP-I(6 h), GZP-II, and GZP-III, respectively. For the preparation of ternary composite, the used oxidant (ammonium peroxysulphate (APS)) concentration was kept constant to observe the growth of polyaniline on the binary composite surface.

The as prepared GZP nanocomposites were characterized by using field emission scanning electron microscopy (FESEM) and transmission electron microscopy (TEM), as shown in **Figures 1**, **2**. As can be seen in the figures, a unique vertically aligned PANI has been successfully grown on GZ composite and the morphology of the PANI can be tuned by using different concentration of monomer. As confirmed by FESEM images (Figure 1A,B,D,F), the nanofibers are 200 nm–2 μm in range. Figure 1A represents the PANI protuberances grown on GZ after 3 h stirring. After 6 h stirring the oriented growth of the protuberances PANI leads to the formation of PANI nanofibre with micrometer length (Figure 1B), which closely resembles like the sea anemone (Figure 1C) (for more SEM images, see Supporting Information, Figure S1). Figure 1D represents the PANI nanorods formation in GZP-II and 1E represent the coral like morphology of PANI containing some nanosphere in GZP-III. Figure 1F represents the large area FESEM of GZP-I (6 h). The formation of vertically aligned polyaniline was further confirmed by TEM analysis. From TEM images in Figure 2G–L, sheet morphology of graphene is clearly shown. Figure 2G,H represent the graphene sheet and ZrO_2 coated graphene sheet, respectively. The Figure 2I–L strongly supports the formation of different types of morphology of PANI grown on GZ. The growth of vertically aligned PANI with different morphology on the GZ surfaces can be explained by the following way. The GZ nanocomposite offers numerous active sites for the PANI growth at the very first of the polymerization of aniline monomer due to the electrostatic attraction between anilinium ions and functional groups. The

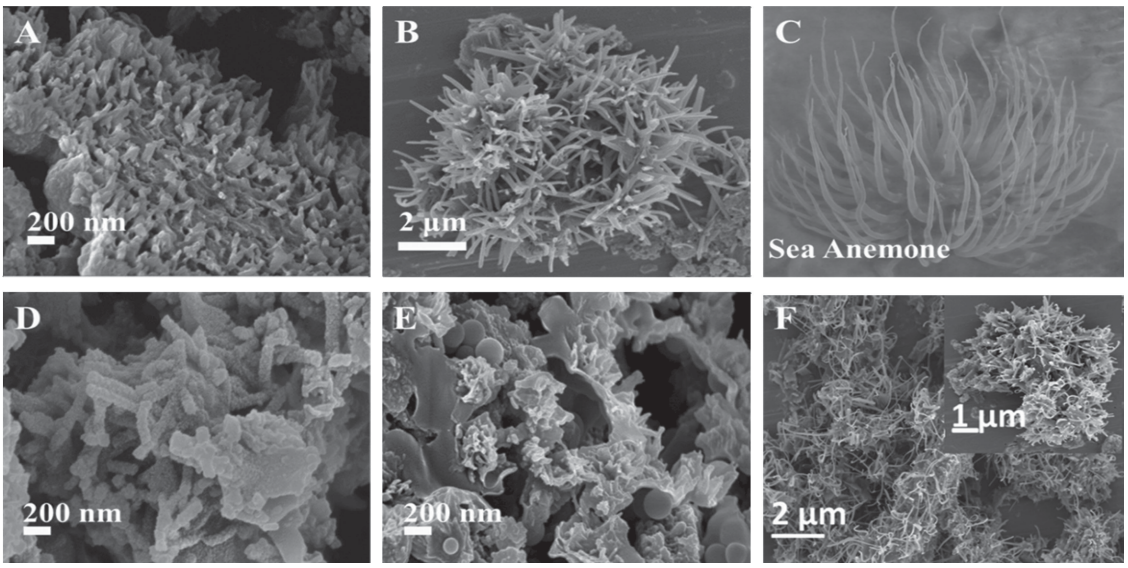

Figure 1. FESEM images of vertically aligned PANI on GZ A) after 3 h stirring, B) after 6 h stirring, C) structure resembles of GZP-I (6 h) a sea anemone, D) PANI nanorod formation of GZP-II, E) PANI nanofiber with nanosphere of GZP-III, F) large scale area of GZP-I (6 h) with magnified view (inset).

precipitation polymerization depends on two important factors: i) Firstly, induction period is switched on and followed by a rapid formation of precipitation; ii) secondly, the surface of the materials strongly influence the progress of the reaction. Noteworthy, polymerization process is achieved firstly on the surface of the seed template. As soon as APS is added into the reaction system, anilinium ions begin to polymerize in these active sites, forming many tiny PANI protuberances on the GZ wall. These protuberances reduce the interfacial energy barrier between the GZ and the other anilinium ions, and also act as the ''seeds'' for further polymerization leading to the formation of vertically aligned PANI. The *in*-situ deposition of fibrillar pernigraniline salt acts as a seed which prompt the continuous seeding process for precipitation and transliterated over many length scales at the nanoscale morphology. In addition, another homogeneous nucleation occurs which results in the production of PANI nanofibers by using aniline micelles as a ''soft template'' in the bulk solution.[11–15] The different shaped polyaniline was obtained for the different GZP composites due to different ratio of ZrO_2 present, which may catalyze the reaction

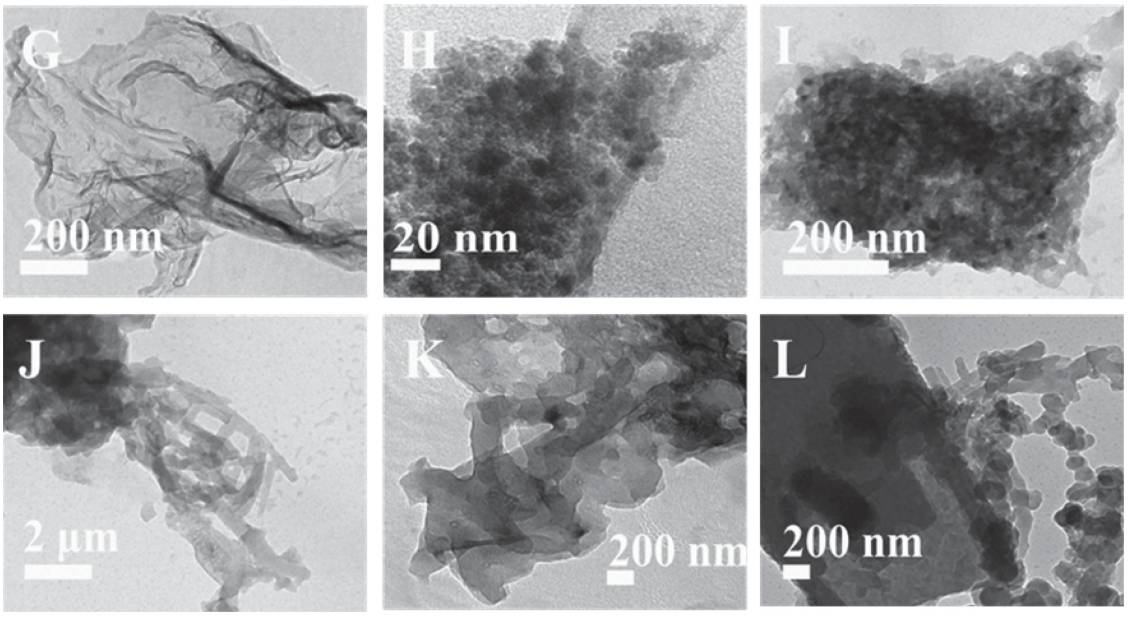

Figure 2. TEM images of G) graphene, H) GZ, I) GZP-I (3 h), J) GZP-I (6 h), K) GZP-II, L) GZP-III.

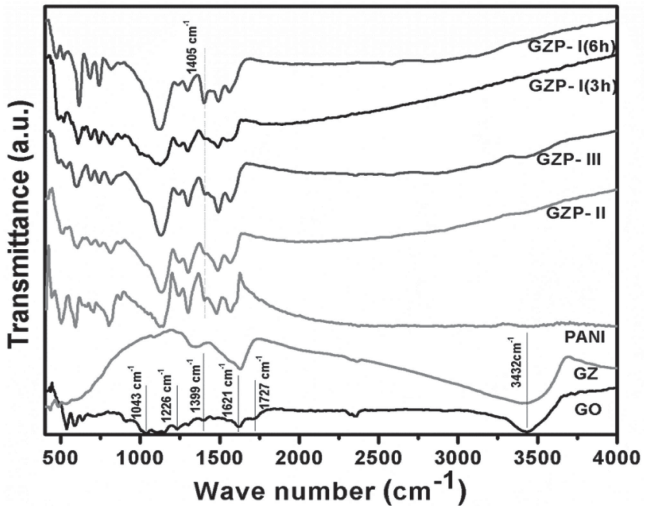

Figure 3. FTIR spectra of the GZP composites in a KBr pellet.

and act as a dopant. When the ZrO_2 to aniline monomer ratio was greater than 1, more aniline monomer formed complex with ZrO_2 forming the sphere shaped protuberances and less amount of aniline were present to diffuse to form elongating. When the dopant and monomer ratio was 0.5, a large number of aniline monomer did not take part in the complex formation instead engaged in elongating the protuberances resulting in the formation of tube like morphology of PANI. When dopant and monomer ratio was 1, PANI with fibriliar morphology was formed and this protuberances combined with initiator solution to produce PANI Nanofibers.[16]

The structures of pristine GO, PANI, GZP composites were characterized by the UV-visible spectroscopy, Fourier transformed infrared (FTIR) spectroscopy, X-ray diffraction (XRD), X-ray photoelectron spectroscopy (XPS), and atomic force microscopy (AFM) analysis. To estimate the band gap of polymer nanocomposites, the UV-visible spectroscopy was studied in DMF solution at the concentration of 0.1 mg mL^{-1}. The band gaps of the as prepared composites are represented in Table S1 (see Figures S2,S3, Supporting Information). Amongst all the composites, (GZP)-I(6 h) exhibited an electrical conductivity of ≈70.8 S cm^{-1}, which was 262 times higher than that of pure PANI (0.27 S cm^{-1}) (see Figure S4, Table S2, Supporting Information).

The FTIR spectra (**Figure 3**) of GO exhibited peaks at 1727 cm^{-1}, 1399 cm^{-1}, 1226 cm^{-1}, and 1043 cm^{-1} representing the C=O stretching of COOH, carboxyl O–H stretching, phenolic C–OH stretching, and alkoxy C–O stretching, respectively. The broad band at 3432 cm^{-1} and the peak at 1621 cm^{-1} are attributed to the H–O–H bending and O–H stretching of the absorbed H_2O molecules, respectively.[17] The FTIR of GZ and GZP exhibited a number of peaks with in the frequency range of 450–520 cm^{-1}, which are the characteristic peaks of Zr–O stretching frequency of ZrO_2. The presence of PANI in all the GZP composites was confirmed from the bands at 1565 and 1488 cm^{-1}, which are associated with the stretching vibration of quinonoid (Q) and benzenoid (B) rings, respectively. The other peaks of GZP at 1299 cm^{-1} and 1243 cm^{-1} can be assigned to the ν_{C-N} in Q–B–Q and B units, and those peaks around 1121 cm^{-1} and 821 cm^{-1} are attributed to the δ_{C-H} in Q and B rings, respectively.[18] The peaks appeared at 650–900 cm^{-1} indicates the C–H out-of-plane deformation vibrations from oligomer like crystal which act as template for further growth of PANI starts. The formation of phenanzine unit which is caused for initiation centers and self-assembling results for further excrescent of PANI chain, is also confirmed from the observed band around 1405 cm^{-1} as reported for the evolution of polyaniline nanotubes by Trchova et al.[19]

The crystallinity study of the nanocomposites was carried out by the XRD analysis and the XRD patterns of all prepared nanocomposites are shown in **Figure 4**. The as prepared GO exhibited a broad peak at 2θ = 12.4° which disappeared in the GZ composite along with the appearance of a new peak around $2\theta = 26.4$, a typical peak corresponding to graphene. In the GZ composites the other peaks appearing at 2θ of 30.4°, 34.8°, 50.42°, 55.57°, 60°, 62.78°, 72.76°, and 75° can be easily indexed as (111), (200), (202), (113), (311), (222), (004), and (400) crystalline plane of tetragonal ZrO_2 (JCPDS PDF No. 02–0733), respectively. The average particle size of the as prepared ZrO_2 nanoparticles in GZ was calculated to be *ca*. 6.6 nm based on Scherrer's equation. The XRD pattern of GZ composite clearly suggests the in-situ reduction of GO to graphene by $ZrO(NO_3)_2 \cdot 3H_2O$, and which oxidized to crystalline ZrO_2 itself. The detailed mechanism of ZrO_2 nanoparticle formation on graphene surface can be proposed which is displayed in the Supporting Information (Figure S5). In the GZP composites, all the peaks of GZ composite retained along with some additional crystallinity introduced, which may be assigned as the crystalline peak of PANI.[20–22] The perpendicular and parallel arrays of PANI growth can be confirmed from the appearances

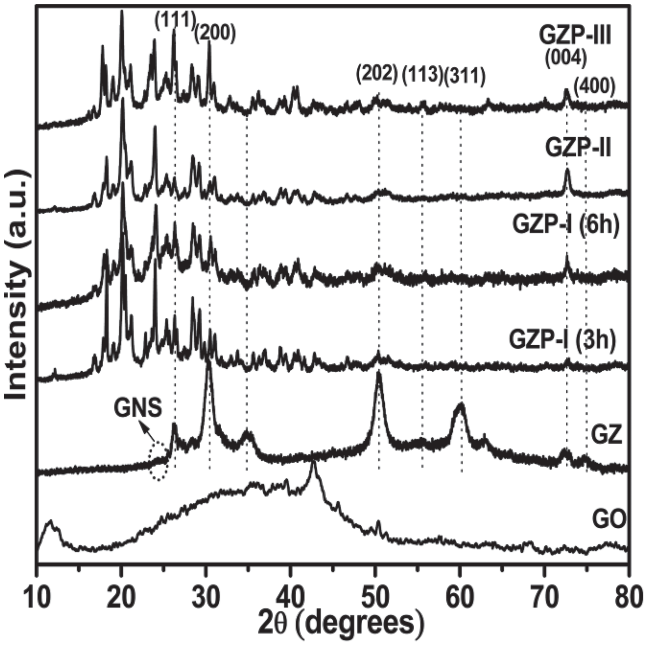

Figure 4. Powder XRD analysis of GZP composites.

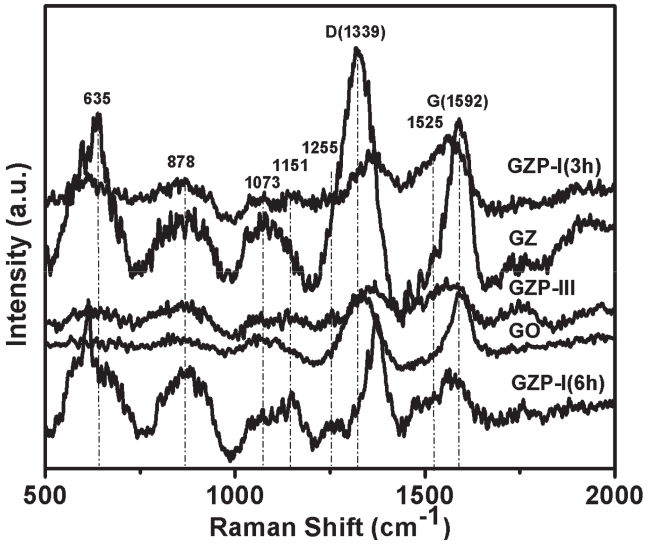

Figure 5. Raman Spectra at 647 nm laser excitation of GZP composites.

of the typical peak at $2\theta = 25.3°$.[20] Polymers are not only grown perpendicular and parallel but also maintain a high oriented alternating distances which is evidenced from the observed peak at $2\theta = 20.3°$. The crystalline peak appeared at $2\theta = 26.4°$ in GZP composites follow the following order (GZPII < GZP I (3h) < GZP I (6 h) < GZPIII) which can be attributed to the gradual increasing amount of GZ ratio accompanied with the polymerization time indicating that graphene becomes incorporated into the nanocomposites with the increasing polymerization time.[23]

To understand the structural property of the as prepared nanocomposites, the Raman studies were performed which are displayed in the **Figure 5**. The Peaks between 500–1200 cm^{-1} are mainly due to the presence of ZrO_2.[24] The Raman peaks at 1339 and 1592 cm^{-1} are attributed to the defect-induced D band arising due to the double-resonance excitation of phonons close to the K-point in the Brillouin zone and the G band arising from the optical E_{2g} phonons at the Brillouin zone center, respectively. The appearance of the G-mode in the range of 1582–1592 cm^{-1} for all the GZ and GZP composites indicates the thin layer of the as prepared graphene. A red shifting of the G band can be observed for the GZP composites in presence of electron donating PANI. The extent of more shifting of the G-peak towards lower frequencies indicates the more electron donating units attached with the GZ. The D/G intensity ratio of GZP-I (6 h) increased as compared to D/G intensity ratio of GZ which suggests that more sp^2 domains are formed during the formation of PANI on GZ. The Raman spectra of the GZP composites at about 1550–1595 cm^{-1}, 1470–1495 cm^{-1}, 1326–1368 cm^{-1}, 1073–1160 cm^{-1}, 1270 cm^{-1}, can be attributed to the C=C quinoid stretching, C=N quinoid stretching, C–N^+ stretching, C–N benzenoid stretching and C–H benzenoid or quinoid stretching of the PANI unit, respectively.[25] The other peaks appeared at 635 cm^{-1} and 878 cm^{-1} are due to the benzenoid ring in plane deformation. The peak observed at 1525 cm^{-1} is due to the NH bending.[26]

To evaluate the thickness of graphene in the as prepared nanocomposites, we have studied the AFM measurements which are shown in the ESI (Figure S6, Supporting Information).

The chemical structure of the GZP composites was studied by XPS analysis and the plots are displayed in **Figure 6**. The wide range spectra of the GZP-I (6 h) composite confirms the presence of C_{1s} (53.32%), N_{1s} (6.89%), Zr_{3d} (3.70%), and O_{1s} (36.09%), respectively. the N and Zr element are attributed to PANI and ZrO_2, respectively. In the wide range spectra both the GZ and GZP-I (6 h) composites (Figure 6A) exhibited two strong peaks at binding energy of 284.6 eV and 529.1 eV corresponding to C1s and O 1s, respectively of the graphene with oxygen containing functional group. From the Figure 6B,C, we can observe the Zr $3d_{5/2}$ peak at 183.7 eV of GZ shifts to 182.9 for GZP-I (6 h) which indiates the electrostatic force of attraction between the electron clouds of the zirconium and nitrogen atoms of PANI, and also confirms the π–π stacking of PANI with graphene. These results clearly demonstrate that ZrO_2 nanoparticles have enhanced the interfacial interactions in the composite. Two peaks (Figure 6C) at 183.7 eV and 186.1 eV of GZP-I (6 h) are attributable to $Zr3d_{5/2}$ and $Zr3d_{3/2}$, respectively, which are in good agreement with the energy splitting of the standard spectrum of ZrO_2.[27] The peak-to-peak separation between the $Zr3d_{5/2}$ and $Zr3d_{3/2}$ level is 2.4 eV, and the area ratio of the two peaks is about 1.4, which are approximately the same values as those reported in the XPS spectrum of ZrO_2.[28] The oxidation state of the Zr element is found to be (+4) in GZP-I (6 h) and the peaks centered at 328 eV and 345 eV are due to Zr $3p_{3/2}$ and to $Zr3p_{1/2}$, respectively, similar to those of previously reported tetragonal ZrO_2 nanoparticle.[29] Figure 7D,E shows the C 1s XPS spectra of the GZ and GZP-I (6 h), respectively. The C1s spectra of the GZ composite can be deconvoluted to the binding energies of 284.4 eV, 285.99 eV, 288.59 eV, and 291.77 eV representing the the C=C bonding (sp^2 carbon, C1) in defect-free graphite, C–N or C–OH or C=N bonding (C2), carbonylate C (HO–C=O) or C–N^+(C3) group, and the O–C=O (C4) components, respectively. For the GZP-I (6 h) composite a shifting of the C–OH binding energy peak to 284.6 eV can be observed indicating the increased conjugation offered by the π–π stacking of graphene, ZrO_2, and PANI. The core level XPS spectra of the N1s of PANI in the GZP-I (6 h) composite can be deconvoluted into three Gaussian peaks (Figure 7F) with the binding energy of 398.76, 399.35 and 401.2 eV, which are attributed to the imine-like structure (–C=N–), the neutral and amine-like structure (–NH–) and positively charged structure (–NH+–), respectively.[30] The N^+/N peak intensity ratio (Figure 6F) is nearly to 0.67 in GZP-I (6 h), attributing a high level proton doping in PANI on GZ.[31] Although the doping level of PANI is far less than the maximum dopant content (H^+ dopant attached per repeat mer unit of PANI) it is still higher than that of the electrodeposited PANI, where the doping level was only 0.25. This comparative high doping content indeed plays a crucial role for the enhanced pseudocapacitive performance.[32]

We have carried out the Brunauer–Emmett–Teller (BET) analysis to understand the specific surface area and the porosity distribution of the as prepared GZ and GZP-I (6 h) composites

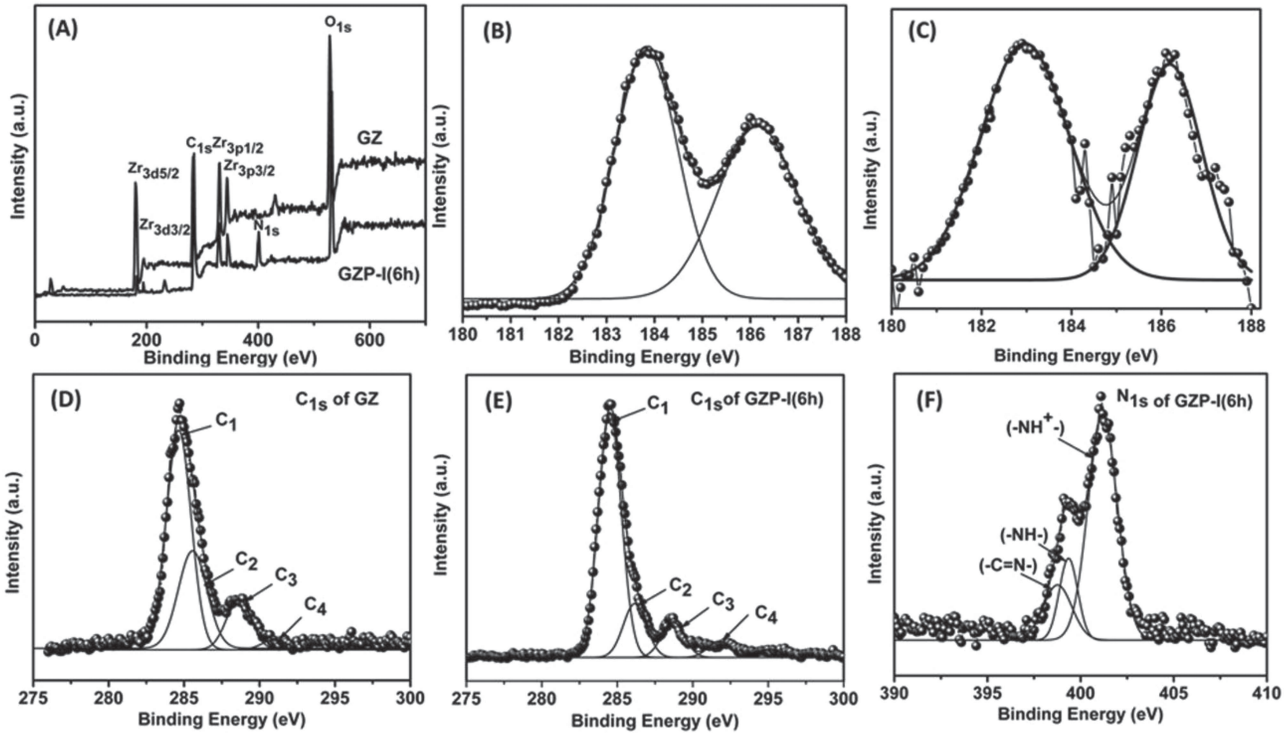

Figure 6. XPS spectra of the GZP-I (6 h), A) GZ nanocomposites survey, B) Zr3d of GZ, C) Zr3d of GZP-I (6 h), D) C1s of GZ, E) C1s of GZP-I (6 h), and F) N1s of GZP-I (6 h).

and the corresponding nitrogen adsorption/desorption isotherm curves and the pore size distribution plots are shown in **Figure 7**. The curves showed the characteristic features of the type-IV isotherm with a H2 (GZP-I (6 h)) and H3 (GZ) hysteresis loop (i.e., the adsorption isotherm is not followed the same path with the desorption isotherm). The type IV isotherm indicates mesoporous characteristics within the nanocomposites. The characteristic H2 and H3 hysteresis loops suggest the presence of many mesoporous adsorbents and the presence of particles giving rise to slit-shaped pore, respectively (Figure 7A and 7C).[33] The rapid increase of the adsorption curve from relative pressure 0.6 for GZP-I (6 h) and 0.85 for GZ reveals the capillary condensation of N_2 gas in the mesopores. The progress of nitrogen adsorption curves increase steeply at relative pressure close to unity, indicating the presence of large interparticle voids. During the pressure change, the hysteresis loop acquires a wide gap suggesting that the mesopores are definitely open which leads to significant delaying between the capillary evaporation and condensation for N_2.[34] The BET surface areas of the GZP-I (6 h) and GZ were calculated to be 207.1 $m^2\ g^{-1}$ and 7.62 $m^2\ g^{-1}$, respectively. The total pore volumes of the GZP-I (6 h) and GZ were 0.3017 cc g^{-1} and 0.0105 cc g^{-1}, respectively. So, the added PANI with the GZ composite increases the specific surface area as well as the pore volume of the GZP-I (6 h) composite. The high surface area and mesoporous structure of GZP-I (6 h) suggests enhanced electrode-electrolyte interface and is beneficial for electrolyte access. Hence, improved electro-chemical performances of electrode materials can be expected.[35]

2.2. Electrochemical Properties of GZ and GZP Composites

CV, EIS, and galvanostatic charge/discharge measurements were performed to explore the advantages of ternary composites containing vertically align polyaniline on GZ surface as electrochemical electrode using a three-electrode cell in 1 M H_2SO_4 electrolyte. **Figure 8** shows the scan rate-dependent CV plots for all the composites at the scan rate of 1 and 2 mV s^{-1}, with a potential window of 0–0.8 V versus a saturated calomel electrode (SCE). The used mass was 0.10 mg. The specific capacitances are calculated by integrating the area of the plot using[32]

$$C_s = \frac{C}{m} = \frac{\int_{V_2}^{V_1} i\,(V)\,\mathrm{d}V}{(V_1 - V_2)\,vm} \tag{1}$$

Where the term in the numerator, of above eq., represents the area of *I*–*V* curve and V1, V2 are the switching potential in cyclic voltammetry and m is the mass (0.10 mg) of all composites and the results are displayed in **Table 1**. Amongst all the composites, the GZP-I (6 h) exhibited highest specific capacitance of 1359.99 F g^{-1} at 1 mV s^{-1}. The CV plots of GZP composite (Figure 8A–D) and GZ (Figure S7, Supporting Information) show roughly a rectangular shape with a pair of small redox peak. The redox peaks pair of GZP composite can be attributed to the interconversion between semiconducting leucoemeraldine state and conducting polaronic state of PANI. It means the capacitance of GZP in H_2SO_4 aqueous electrolyte mostly comes from the pseudocapacitance arising from the redox reactions

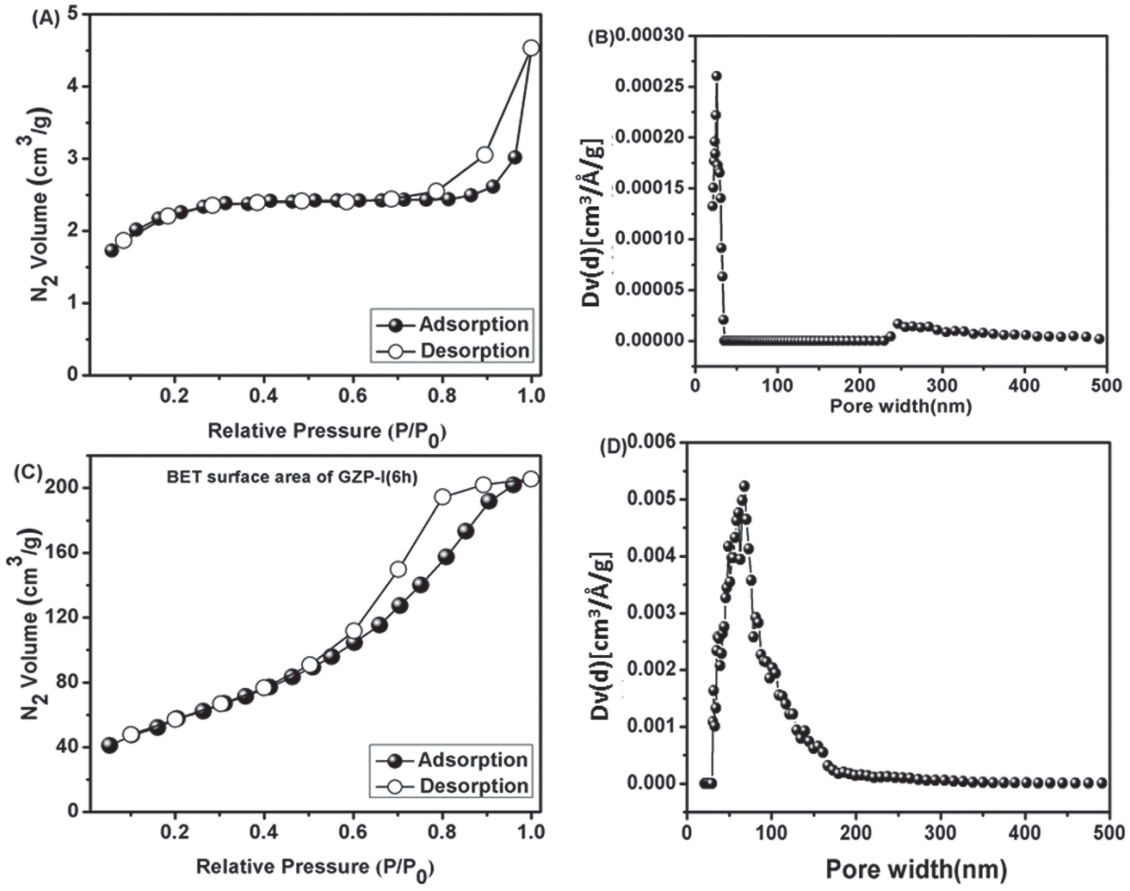

Figure 7. Nitrogen adsorption/desorption isotherms demonstrate the mesoporous structure of A) GZP-I (6 h) and C) GZ, B) The corresponding pore size distribution of GZP-I (6 h) and D) for GZ.

occurring within the vertically align PANI and the redox active ZrO_2 accompanied with the electrical double layer capacitance at the electrode/electrolyte interface of the host GZ material. The better electrochemical stability of the double layer capacitor compared to pseudocapacitors and in contrary the better charge storage ability of the pseudocapacitors over the double layer capacitors are the main motivations to combine both type of materials in a single composite to obtain a hybrid material which can have both good specific capacitance and excellent electrochemical stability. The arrays of vertically aligned PANI over the GZ surface acts as a pseudocapacitance source and also play a major role in increasing the specific capacitance of the hybrid composite both by providing high contact area with the electrolyte and shortening the electronic or electrolyte ion transport path lengths.

It clearly indicates that the increment of GZ ratio in the nanocomposite improves the total capacitance by enhancing the EDLC contribution, the agglomeration of graphene nanosheets was minimized and improved permeation of electrolyte was achieved. No obvious distortion was observed with increasing the scan rate and the roughly rectangular shape was well maintained indicating that the GZP nanocomposite has a low equivalent series resistance and a fast kinetics of electrolyte ions diffusion. Two types of mechanisms are involved during charging and discharging of the composites. Firstly, the insertion/extraction of H^+ transpired in the ternary composite during redox process and secondly the H^+ ions chemisorbed on the surface of the matrix rather than bulk. Insertion/extraction of H^+ into/from the polymer as well as oxide framework leads to the charge transfer at the metal oxide sites which generates the pseudocapacitance in the form of hydroxonium ion H_3O^+. The lattice expansion was triggered from not merely surface adsorption, but bulk insertion of cations into the ZrO_2 lattice and the increase in free energy favors the insertion of more H_3O^+.This extent of H_3O^+ accommodation leads to the more capacitance by making more charge transfer tunnels. Further, the sample acts as "ion–buffering reservoirs" for comprising the indefinite numbers of nanochanells and high pore volume which stimulate the faster ionic and electronic kinetics by reducing the mean free path, thus make best use of the reversible insertion/de-insertion of ions.[7]

The embedded ZrO_2 in the ternary composite provides high energy storage capacity by keeping PANI nanofibre from collapsing and aggregating, while the highly conductive PANI nanofibres facilitate the electron transport and easy ion diffusion into the core of ZrO_2. The complementary properties of both components generate a synergistic effect to enhance the electrochemical performance.[36–38] The electrode materials with

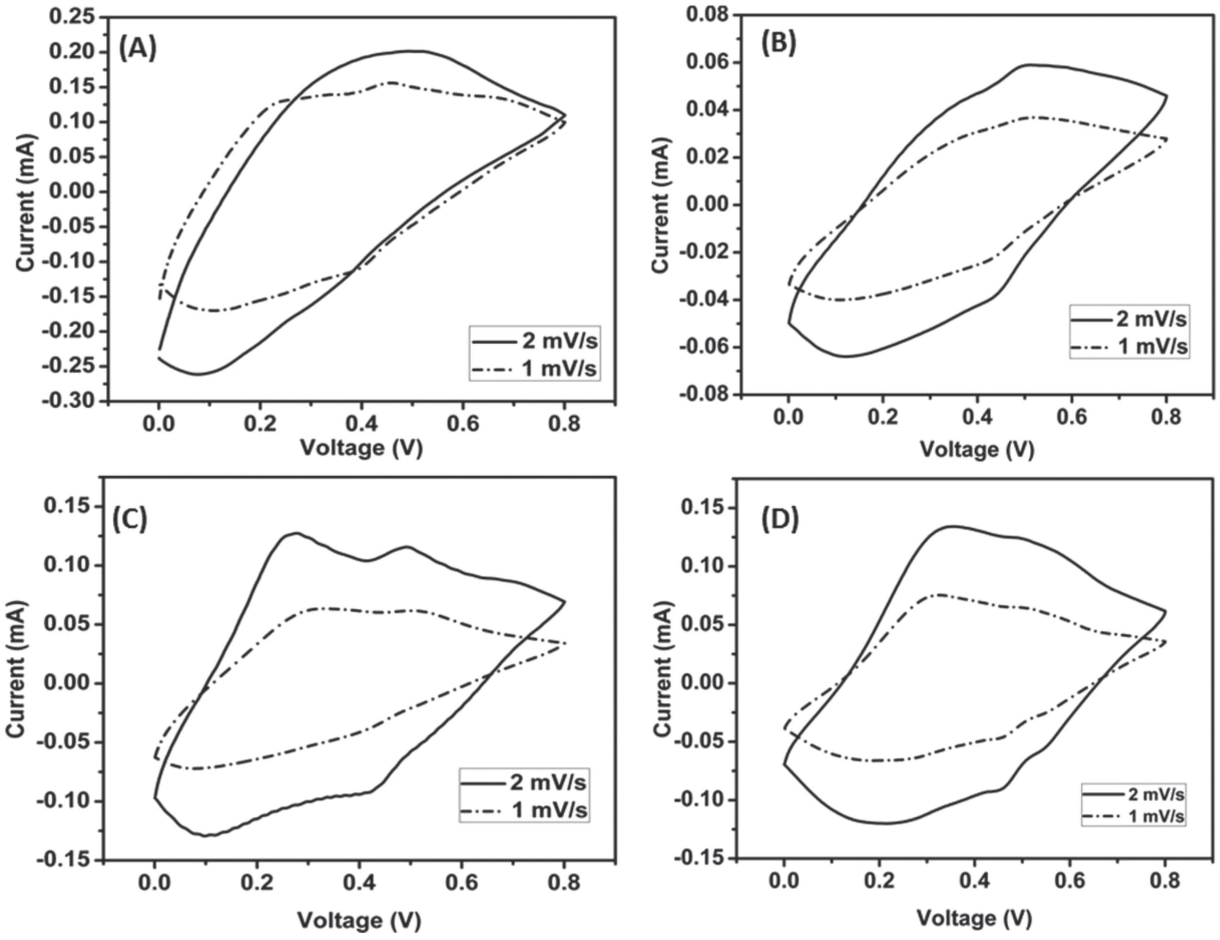

Figure 8. Cyclic voltammetry of A) GZP-I (6 h), B) GZP-I (3 h), C) GZP-II, D) GZP-III were recorded at room temperature at the scan rate of 1 and 2 mV s^{-1}.

high specific surface area and high porosity at the nanoscale level effect the redox behavior of the material by the easy ions transportation through the electrode matrix. Thereby, morphologically preferable vertically align polyaniline with higher dimension contains more surface than bulk which serves numerous number of redox reactions sites providing higher charge storage capacity.

The EIS analysis was performed applying A. C. voltage amplitude of 5 mV within the frequency range of and 0.1 (final) Hz to 10^6 Hz (initial) and the analyzed curves are represented in terms of Nyquist plot in **Figure 9**A. To evaluate the various electrochemical phenomenons occurring within the electrode and the various electrochemical parameters involved in it. The Nyquist plots were fitted with an equivalent electrical circuit (Figure 10) and the interpreted data are shown in **Table 2**. In the circuit the terms R_s, R_{ct}, W_d, and C_{dl} represent the solution resistance, charge transfer resistance of the faradic process, Warburg coefficient and double layer capacitance, respectively (Figure 9D). Figure 9A,B clearly demonstrate the lowest R_s of 18 Ω for the GZP-I (6 h) composite and the highest R_s of 19.13Ω for the GZP-I (3 h) composite. The high frequency semicircle in the Nyquist plot can be attributed to the discontinuity in the charge transfer process (R_{ct}) due to the conductivity difference between the solid oxide (electronic conductivity) and liquid electrolyte phase (ionic conductivity). The higher the semicircle radius, the higher will be the charge transfer resistance. At the lower frequency region the linear part of the Nuquist plot represents the diffusion-limited electron transfer process (W_d). The more vertical the curve corresponding to a cell, the closer it is to an ideal capacitor. The Warburg resistance is generated by the interruptions in the sample uniformity during diffusion process i.e. during the semi-infinite diffusion of ions into the porous structure. The Warburg like arc might

Table 1. Calculated specific capacitance by integrating the area of the curve.

Sample	C_s [F g^{-1}] at 1 mV s^{-1}	C_s [F g^{-1}] at 2 mV s^{-1}
GZP-I (6 h)	1359.99	922
GZP-I (3 h)	430.07	352
GZP-II	896	768.5
GZP-III	830.25	766.3
GZ	317.5	203.1

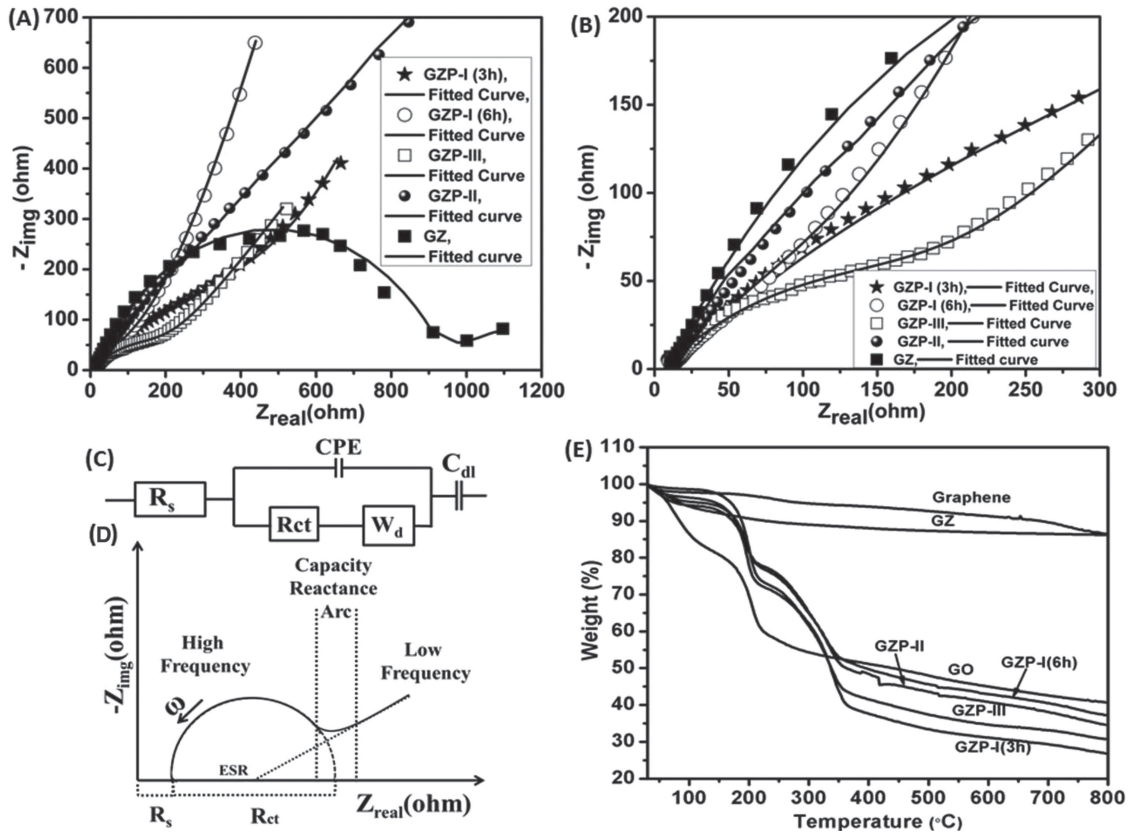

Figure 9. A) Nyquist plots (10^6–0.1 Hz) of GZ and GZP composites, B) high-frequency region Nyquist plots, C) Modeled equivalent circuit of EIS where R_s stands for the electrolyte resistance, R_{ct} the charge transfer resistance, W_d the "Warburg" resistance, CPE the constant phase element, and C_{dl} the potential-dependent capacitance, D) Schematic of EIS, E) Thermogravimetry analysis (TGA) of GZP composites.

be generated from the ambipolar equilibrium inside the composites.[7,39] The equivalent series resistance (ESR), which is a measure of conductivity interms of resistance of an electrode material, can be calculated from the tangential intersection of the corresponding Nyquist plots on Z_{real}–axis.[7] The ESR values of the GZ, GZP-I (6 h), GZP-I (3 h), GZP-II, and GZP-III composites were found to be 820 Ω, 15.12 Ω, 150.4 Ω, 26.79 Ω, and 47.75 Ω, respectively. These values clearly prove the higher conductivity of polyaniline nanofiber containing GZP-I (6 h) and sequentially reflect the better accommodation and transportation of cations in the GZP composite. Easy ionic conduction/transportation throughout the polymer matrix as well as bulk ZrO_2 is also essential for improvement of the pseudocapacitive performance. In addition, ionic conductivities were also influenced by the H_3O^+ incorporation in the constituents of GZP composites; the higher water content stimulates proton hopping throughout the sample matrix.

The thermogravimetry (TGA) curve of the GZP composites exhibited mainly three stages of weight loss with the temperature range of 30–800 °C. The first stage of weight loss upto 100–120 °C can be attributed to the loss of adsorbed water molecule. The highest weight loss occurred for the GZP-I (6 h) within this range indicating the most surface adsorbed water molecules which indeed increase the proton conductivity

Table 2. The EIS fitted data by a suitable equivalent circuit fitting.

Sample Name	R_s [Ω]	R_{ct} [Ω]	CPE [Siemens × Second^n]	a = n (0 < n < 1)	W_d [Siemens × Second$^{1/2}$]	C_{dl} (F)
GZP-I(6 h)	18.0	132.4	99.6×10^{-6}	0.683	603×10^{-6}	386.7×10^{-6}
GZP-I(3 h)	19.13	250.5	281×10^{-6}	0.429	752×10^{-6}	518×10^{-6}
GZP-II	18.951	180.6	137×10^{-6}	0.456	760×10^{-6}	57×10^{-9}
GZP-III	18.12	249.7	120.4×10^{-6}	0.461	765.6×10^{-6}	52×10^{-9}
GZ	10.06	840.3	0.120×10^{-3}	0.377	780.2×10^{-6}	4.7×10^{-9}

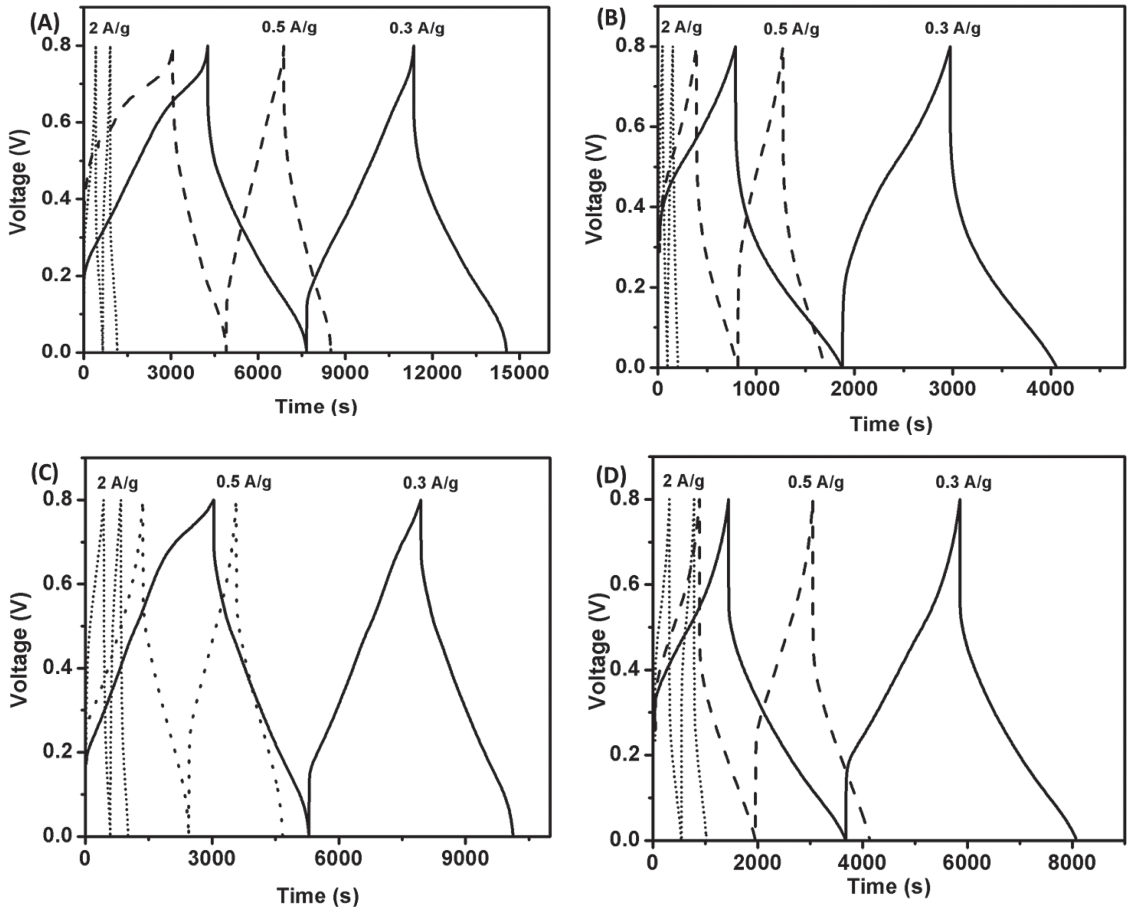

Figure 10. The galvanostatic charge–discharge of the A) GZP–I (6 h), B) GZP-I (3 h), C) GZP-II, and D) GZP-III at the current density of 0.3, 0.5, 2 A g^{-1}.

during charging/discharging process. The 2nd stage of weight loss of the composites occurs around 270 °C, which is mainly due to the loss of unbounded dopant and oligomers degradation of PANI. Third weight loss occurs around 369 °C which is due to the loss of the bounded dopant and thermal oxidative decomposition of the nanocomposites, respectively.[40] In contrary to the previous observance, the least weight loss occurred for the GZP-I (6 h) at this stage. This behavior of GZP-I (6 h) indicates that the PANI strongly interacts with the ZrO_2 unit as well as the graphene surface which also increase the ionic and electrical conductivity of the composite than the other composites.

The galvanostatic charge–discharge method was performed at different current densities of 0.3, 0.5, and 2 A g^{-1} for the reliability and possible application of supercapacitor electrode materials under controlled conditions. **Figure 10**A–D clearly show that the time duration of charging/discharging increases with decrease in current density, which leads to the higher specific capacitance by lowering the resistivity of the electrode. The specific capacitance from the discharging time was calculated (see **Table 3**) by using

$$C_s = \frac{I \times t}{V \times m} \tag{2}$$

Where I/m is the used current density, t is time for discharging, V is the potential window. The energy density and power density are the two key factors for application in the energy storage system of electrochemical supercapacitors. The energy density (E) and power density (P) of the composites were calculated by using the following equations

$$E = \frac{1}{2} C_s V^2 \tag{3}$$

and

$$P = \frac{E}{t} \tag{4}$$

Table 3. Specific capacitance (F g^{-1}) calculated from charge-discharge measurements.

Sample	C_s [F g^{-1}] at 0.3 A g^{-1}	C_s [F g^{-1}] at 0.5 A g^{-1}	C_s [F g^{-1}] at 2 A g^{-1}
GZP-I (6 h)	1178.6	968.75	675
GZP-I (3 h)	407	267.5	128.75
GZP-II	832.12 A g^{-1}	676.6	590
GZP-III	817.6	688.12	462.5

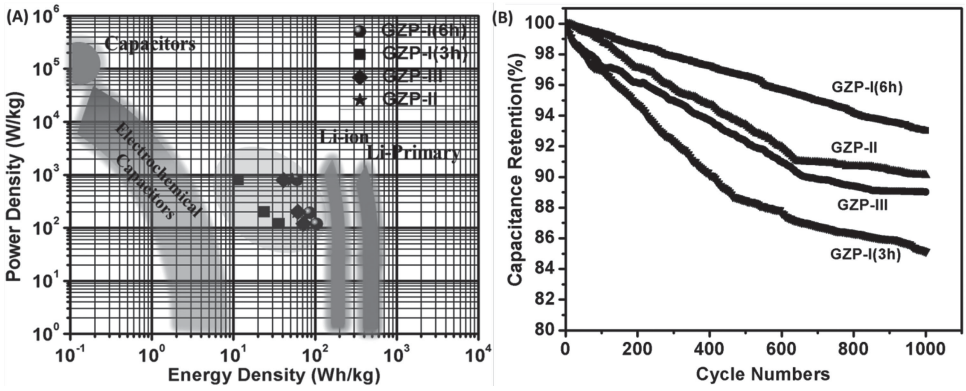

Figure 11. A) The power density versus energy density of GZP composites in a Ragone plot for conventional batteries, conventional capacitors, and normal ultracapacitors,[1] B) % capacitance retention with cycle number (1000 cycles) of the GZP composites, derived from the chronopotentiometry study.

where V is the potential window, E is the energy density, t is the discharging time. **Figure 11**A shows the energy density vs. power density curve in terms of Ragone plot. The highest energy density of 104.76 Wh kg^{-1} at a power density of 0.118 kW kg^{-1} was obtained for the GZP-I (6 h). On the other hand the highest energy density 41.11 Wh kg^{-1} was shown by GZP-III at a power delivery rate of 0.8 kW kg^{-1}. These various energy density and the corresponding power density values (**Table 4** and **5**) were much higher than those of conventional supercapacitors. The charge-discharge efficiency of the GZP composites were found to be 85%, 96%, 99%, and 103% for the GZP-I (6 h), GZP-I (3 h), GZP-II, and GZP-III, respectively. The high Coulombic efficiency clearly demonstrates the high rate control capability and electrochemical reversibility of the electrode materials.[41] The cycle stability of the hybrid composites was examined at a current density of 0.3 A g^{-1} and the specific capacitance retention of 93.02%, 85.12%, 89.01%, 90.11% were recorded for the GZP-I (6 h), GZP-I (3 h), GZP-II, and GZP-III, respectively. The capacitance decay can be explained by considering the following two factors. Firstly, the irreversible reaction between the electrodes and electrolyte caused by the consumption of electrolyte, and secondly, the poor cyclic stability of conducting polymers (PANI) due to the swelling and shrinking during the charge–discharge (doping–dedoping), a consequence of the cyclic mechanical stress effect.[42]

These high electrochemical performances of GZP composites maintained the following aspects: 1) the metal oxide nanoparticles are well dispersed throughout the graphene surface and vertically align polyaniline inhibited the restacking of graphene sheets. 2) The vertically alignment of polyaniline chain results in an good contact with electrolyte which enhanced electrical double layer capacitance as well as shorten the diffusion and migration of electrolyte ions. 3) The presence of metal oxide highly influences the overall specific capacitance by contributing the ion hopping though out the composite matrix. 4) With the incorporation of graphene layer into the composites, the high chemical stability with high electrical conductivity are well maintained due to strong interation with PANI chain through ZrO_2 metal oxide bridges, which enhances the accessibility of the eletrolyte ions. 5) the hierarchical PANI unit providing more redox active sites due to its unique vertical arrangement, high surface area, narrow pore size distribution with short pore length facilitates quick ions transport, resulting in the formation of huge number of electrical double layers in terms of charge storage all over the composites. These combination of interesting results endowed its suitability for practical application of high-performance electrochemical energy storage devices.[43]

3. Conclusions

A novel synthetic route was followed for the development of durable asymmetric supercapacitor based on graphene, ZrO_2, and most interestingly the vertically aligned PANI. The morphology and the alignment of PANI can be changed by simply changing the aniline monomer to Graphene/ZrO_2 composite ratio and the polymerization time. For the first time, vertically

Table 4. Calculated energy density (Wh kg^{-1})from charge-discharge measurements.

Sample	*E* [Wh kg^{-1}] at 0.3 [A g^{-1}]	*E* [Wh kg^{-1}] at 0.5 [A g^{-1}]	*E* [Wh kg^{-1}] at 2 [A g^{-1}]
GZP-I (6 h)	104.76	86.11	60
GZP-I (3 h)	36.17	23.77	11.45
GZP-II	73.96	60.14	52.44
GZP-III	72.67	61.66	41.11

Table 5. Calculated power density (W kg^{-1}) from charge-discharge measurements.

Sample	*P* [W kg^{-1}] at 0.3 [A g^{-1}]	*P* [W kg^{-1}] at 0.5 [A g^{-1}]	*P* [W kg^{-1}] at 2 [A g^{-1}]
GZP-I (6 h)	118.07	190.76	800
GZP-I (3 h)	120.45	200.96	796.67
GZP-II	119.98	199.91	803.33
GZP-III	120.11	201.7	800.84

align PANI were grown on the metal oxide surface which was synergistically attached with graphene surface and provided the supercapacitor with much improved performances. These materials can be cycled reversibly in the voltage range of 0–0.8 V, and exhibited the maximum specific capacitance of 1178.6 F g^{-1} at the current densities of 0.3 A g^{-1}. The maximum energy density of 104.76 Wh kg^{-1} and maximum power density of 0.8 kW kg^{-1} were achieved. Moreover, the electrode materials exhibited high cyclic stability and highest 93.02% specific capacitance retained for GZP-I (6 h) after 1000 cycles. We believe, this designed concept would be the new opportunities in the field of another energy storage devices containing different type of metal oxide.

4. Experimental Section

Preparation of GZ Composite: Graphene oxide was prepared by modified hammers method.[1,44] At first, 60 mg of GO was added in 30 mL of $ZrO(NO_3)_2{\cdot}3H_2O$ (0.3 M) aqueous solution with vigorous stirring. After being ultrasonicated for 2 h, the black solution was transferred to a round bottom flask and reflux the mixture with constant stirring at 120 °C for complete reduction of graphene oxide by $ZrO(NO_3)_2{\cdot}3H_2O$ for 24 h in N_2 atmosphere. Thereafter, the solution mixture was put into a stainless steel Teflon-lined autoclave of 50 mL capacity and maintained for 12 h at 150 °C. The pH of the mixture was maintained about 8 by adding NH_4OH (3 mL). The product was filtered and washed with deionized water and ethanol repetedly and dried at 60 °C for one day under vacuum.

Preparation of GZP Composites: Taking 60 mg of GZ composite in 50 mL (0.5 M) HCl, monomer concentration was varied with GZ as (1:1), (0.5:1), and (1:0.5). The APS (2 gm) concentration was kept constant to synthesize all the GZP composites. The APS was added drop by drop maintaining the temperature at 0–5 °C for 6 h with constant stirring at 500 rpm. The color change of violet to greenish was observed. To understand the mechanism of PANI formation we took away little amount of the product from the reaction mixture at the time of 3 h and the stirring was continued up to 6 h. The different time polymerized composites were washed several times with deionized water and centrifuged. The products are kept at 60 °C for 48 h under vacuum.

Characterizations: CV, EIS, and galvanostatic charge/discharge measurements were performed using a potentiostatic electrochemical workstation (VMP3, Bio-Logic, France). The UV–visible spectra were carried out using PERKIN-ELMER instrument by dispersing the sample (concentration-0.1 mg mL^{-1}) in dimethyl formamide (DMF). FTIR spectra were recorded by NEXUS 870 FT-IR (Thermo Nicolet) instrument by making a pellet of the sample. Raman spectroscopy was studied using Bruker Raman spectrometer at an excitation wavelength of 647 nm. XRD measurements were carried out by Rigaku X-ray diffractometer, ULTIMA-III with Cu Kα source (λ = 1.5418 Å). The X-ray photoelectron spectroscopic (XPS) study was performed for the samples using the Kratos Axis-ULTRA XPS analyzer. The X-ray source used was a monochromatic Al Kα line ($h\upsilon$ = 1486.71 eV) powered with 10 mA and 15 kV. It was carried out after a plasma cleaning at the XPS chamber pressure of about 4×10^{-8} Torr for 300 s. The specific surface area and pore structure were investigated using a Quantachrome Instrument using nitrogen as the adsorbate at 77 K. FESEM images were obtained using Carl Zeiss-SUPRATM 40 FESEM instrument to understand the morphology. TEM were carried out on JEOL 2100 TEM instrument. Dupont 2100 thermogravimetric analyzer was used for measuring the weight loss of the sample. The AFM studies of the samples were performed by NT-MDT and Veeco Nanoscope instruments.

Electrode Fabrication and Electrochemical Measurements: For electrochemical measurements, 0.1 mg of the sample was completely dispersed into 1% nafion solution (which has very negligible effect on capacitance[2,45] and ultrasonicated for 10 min. The prepared solution was cast onto the glassy carbon electrode (diameter-3 mm). After that this glassy carbon electrode was completely dried in vacuum oven at 40 °C and used as a working electrode. The saturated calomel electrode and platinum foil were used as reference and counter electrode, respectively. The measurements were investigated in a 1 M H_2SO_4 aqueous electrolyte at room temperature. CV was performed between 0 V to + 0.8 V versus SCE at the scan rate of 1 and 2 mV s^{-1}. Cyclic charge–discharge test (CCD) was performed at a current density of 0.3–2 A g^{-1}. Electrochemical impedance spectroscopy (EIS) was also tested within the frequency range of 10^6 (initial) and 0.1 (final) Hz.

Supporting Information

Supporting Information is available from the Wiley Online Library or from the author.

Acknowledgements

The authors would like to specially thank the CSIR, New Delhi, India for their financial support. The authors are also thankful to IIT Kharagpur for providing the instrumental facilities. Authors are thankful to Mr. Arnab Maity, IISER, Kolkata and Mr. Rishi Maiti, IIT Kharagpur, India, for AFM measurements and interpretations. Authors are grateful to Mr. Debabrata Nandi for conductivity measurements and discussions. The Sea anemone picture was taken at the Chandipur Sea beach, Orissa, India.

Received: June 25, 2013
Revised: August 9, 2013
Published online: October 30, 2013

[1] P. Simon, Y. Gogotsi, *Nat. Mater.* **2008**, *7*, 845.
[2] Y. Li, Z. Li, P. Kang Shen, *Adv. Mater.* **2013**, *25*, 2474.
[3] Y. Zhu, S. Murali, M. D. Stoller, K. J. Ganesh, W. Cai, P. J. Ferreira, A. Pirkle, R. M. Wallace, K. A. Cychosz, M. Thommes, D. Su, E. A. Stach, R. S. Ruoff, *Science* **2011**, *332*, 1537.
[4] J. R. Miller, P. Simon, *Science* **2008**, *321*, 651.
[5] Y. Zhu, S. Murali, W. Cai, X. Li, J. W. Suk, J. R. Potts, R. S. Ruoff, *Adv. Mater.* **2010**, *22*, 3906.
[6] L. Zheng, Y. Xu, D. Jin, Y. Xie, *Chem. Asian J.* **2011**, *6*, 1505.
[7] S. K. Meher, G. R. Rao, *J. Power Sources* **2012**, *215*, 317.
[8] Y. S. Yun, S. Youn Cho, J. Shim, B. H. Kim, S. J. Chang, S. J. Baek, Y. S. Huh, Y. Tak, Y. W. Park, S. Park, H. J. Jin, *Adv. Mater.* **2013**, *25*, 1993.
[9] H. J. Shin, K. K. Kim, A. Benayad, S. M. Yoon, H. K. Park, I. S. Jung, M. H. Jin, H. K. Jeong, J. M. Kim, J. Y. Choi, Y. H. Lee, *Adv. Funct. Mater.* **2009**, *19*, 1987.
[10] J. Lu, J. B. Zang, S. X. Shan, H. Huang, Y. H. Wang, *Nano Lett.* **2008**, *8*, 4070.
[11] J. Xu, K. Wang, S. Z. Zu, B. H. Han, Z. Wei, *ACS Nano* **2010**, *4*, 5019.
[12] Z. M. Zhang, Z. X. Wei, M. X. Wan, *Macromolecules* **2002**, *35*, 5937.

[13] N. R. Chiou, A. J. Epstein, C. Lu, J. Guan, L. J. Lee, *Nat. Nanotechnol.* **2007**, *2*, 354.
[14] L. Liang, J. Liu, C. F. Windisch, G. J. Exarhos, Y. Lin, *Angew. Chem. Int. Ed.* **2002**, *41*, 3665.
[15] J. Liu, Y. Lin, L. Liang, J. A. Voigt, D. L. Huber, Z. R. Tian, E. Coker, B. Mckenzie, M. J. Mcdermott, *Chem. Eur. J.* **2003**, *9*, 604.
[16] C. A. Amarnath, J. Kim, K. Kim, J. Choi, D. Sohn, *Polymer* **2008**, *49*, 432.
[17] X. Wanga, H. Tian, Y. Yang, H. Wang, S. Wang, W. Zheng, Y. Liu. *J. Alloys Comp.* **2012**, *524*, 5.
[18] H. Liu, X. B. Hu, J. Y. Wang, R. I. Boughton, *Macromolecules* **2002**, *35*, 9414.
[19] M. Trchová, I. Šeděnková, E. N. Konyushenko, J. Stejskal, P. Holler, G. Ćirić-Marjanović, *J. Phys. Chem. B* **2006**, *110*, 9461.
[20] J. P. Pouget, M. E. Jozefowicz, A. J. Epstein, X. Tang, A. G. MacDiarmid, *Macromolecules* **1991**, *24*, 779.
[21] Q. Lu, Q. Zhao, H. Zhang, J. Li, X. Wang, F. Wang, *ACS Macro Lett.* **2013**, *2*, 92.
[22] D. Han, Y. Chu, L. Yang, Y. Liu, Z. Lv, *Colloids Surf., A* **2005**, *259*, 179.
[23] Y. Z. Li, X. Zhao, Q. Xu, Q. H. Zhang, D. J. Chen, *Langmuir* **2011**, *27*, 6458.
[24] C. Wulfman, N. Djaker, N. Dupont, D. Ruse, M. Sadoun, M. L. L. Chapelle, *J. Am. Ceram. Soc.* **2012**, *95*, 2347.
[25] R. Liang, H. Cao, D. Qian, J. Zhangc, M. Qu, *J. Mater. Chem.* **2011**, *21*, 17654.
[26] M. Jain, S. Annapoorni, *Synth. Met.* **2010**, *160*, 1727.
[27] *Handbooks of Monochromatic XPS Spectra*, (Ed: B. V. Crist), Vol. *2*, Commercially Pure Binary Oxides, XPS International LLC, USA **2001**, p 830.
[28] Y. Shan, Lian Gao, *Nanotechnology* **2005**, *16*, 625.
[29] Yeonmi Shin, Seonghoon Lee, *Nanotechnology* **2009**, *20*, 105301.
[30] J. Wang, Y. Xu, J. Zhu, P. Ren, *J. Power Sources* **2012**, *208*, 138.
[31] B. J. Kim, S. G. Oh, M. G. Han, S. S. Im, *Langmuir* **2000**, *16*, 584.
[32] X. Xia, Q. Hao, W. Lei,W. Wang, D. Suna, X. Wang, *J. Mater. Chem.* **2012**, *22*, 8314.
[33] Z. Ryu, J. Zheng, M. Wang, B. Zhang, *Carbon* **1999**, *37*, 1257.
[34] F. Zhang, H. Cao, D. Yue, J. Zhang, M. Qu, *Inorg. Chem.* **2012**, *51*, 9544.
[35] F. Zhang, T. Zhang, X. Yang, L. Zhang, K. Leng, Y. Huanga, Y. Chen, *Energy Environ. Sci.* **2013**, *6*, 1623.
[36] Z. A. Hu, Y. L. Xie, Y. X. Wang, L. P. Mo, Y. Y. Yang, Z. Y. Zhang, *Mater. Chem. Phys.* **2009**, *114*, 990.
[37] Y. Yan, Q. Cheng, V. Pavlinek, P. Saha, C. Li. *Electrochim. Acta.* **2012**, *71*, 27.
[38] R. Liu, J. Duay, T. Lanea, S. B. Lee, *Phys. Chem. Chem. Phys.* **2010**, *12*, 4309.
[39] P. Jasinski, V. Petrovsky, T. Suzuki, H. U. Anderson, *J. Electrochem. Soc.* **2005**, *152*, J27.
[40] T. Jeevananda, T. S. Lee, J. H. Lee, O. M. Samir, R. Somashekar, *J. Appl. Polym. Sci.* **2008**, *109*, 200.
[41] X. Xia, Q. Hao, W. Lei, W. Wang, H. Wang, Xin Wang, *J. Mater. Chem.* **2012**, *22*, 8314.
[42] M. Zhang, K. R. Atkinson, R. H. Baughman, *Science* **2004**, *306*, 1358.
[43] Z. Fan, J. Yan, T. Wei, L. Zhi, G. Ning, T. Li, F. Wei, *Adv. Funct. Mater.* **2011**, *21*, 2366.
[44] D. C. Marcano, D. V. Kosynkin, J. M. Berlin, A. Sinitskii, Z. Sun, A. Slesarev, L. B. Alemany, W. Lu, J. M. Tour, *ACS Nano* **2010**, *4*, 4806.
[45] F. Lufrano, P. Staiti, M. Minutoli, *J. Electrochem. Soc.* **2004**, *151*. A64